Constraints on yield strength in the oceanic lithosphere derived from observations of flexure

Marcia K. McNutt* *United States Geological Survey, 345 Middlefield Road, Menlo Park, California 94025, USA*

H. W. Menard *Geological Research Division, Scripps Institution of Oceanography, La Jolla, California 92093, USA*

Summary. The wavelength and amplitude of outer rises seaward of subduction zones and arches surrounding islands and seamounts are used to parameterize flexure profiles in terms of the moment and curvature at the first zero crossing. The data show the clear age dependence in the mechanical thickness of the lithosphere up to 60–100 Myr. Saturation of moment at large curvature is interpreted in terms of a depth-dependent yield strength for the lithosphere using relations adopted from laboratory experiments of rock deformation. A comparison of theoretical curves with observed moments indicates that old oceanic lithosphere has no long-term strength below about 40 km depth, with no difference between 100 and 165 Myr old crust. Moderate axial loading forces (± 200 MPa) can explain most variations in the moment/curvature observations, except in the case of the Kuril Trench which appears anomalous given the age of the crust. Regional tension causes greater variability in moment as compared to regional compression because of the greater slope in the brittle failure envelope under tension. The observations point to a lithosphere weaker than the prediction from experimental deformation of rocks. Of the possible weakening mechanisms, elevated pore-fluid pressure on faults does not predict the correct age dependence and is incompatible with earthquake focal mechanisms. Our favoured explanation is that the activation energy, Q, appropriate for ductile flow at geological strain rates is lower than the values derived from laboratory extrapolations of dry olivine data taken at high temperatures. If recent oceanic geotherms are reliable, Q in the lower lithosphere must be lower than $100 \, \text{kcal mol}^{-1}$. The method used here is most appropriate for trench profiles with curvatures greater than $10^{-7} \, \text{m}^{-1}$. For lower curvatures, such as along seamount profiles, small errors in the curvature estimate cause large changes in rheological parameters.

*Present address: 54-1018 Department of Earth and Planetary Sciences, Massachusetts Institute of Technology, Cambridge, Massachusetts 02139, USA.

Introduction

The bending of the oceanic crust in the vicinity of many islands and seamounts (Vening-Meinesz 1941; Walcott 1970; Watts & Cochran 1974; McNutt & Menard 1978) and seaward of subduction zones (Hanks 1971; Watts & Talwani 1974; Caldwell *et al.* 1976) represents an excellent opportunity to study the deformation of rock at geological strain rates. To a good first approximation, the behaviour of older seafloor when subjected to surface loads, horizontal tension or compression, or applied bending moments is largely elastic with an effective elastic thickness of the lithosphere ranging between about 20 and 40 km. Furthermore, Watts, Bodine & Ribe (1980) have shown that the effective elastic thickness increases roughly as the square root of age of the lithosphere when loaded (Fig. 1). Such a dependence could have been anticipated from plate and half-space cooling models which describe the evolution of the oceanic lithosphere (Turcotte & Oxburgh 1967; McKenzie 1967; Parker & Oldenburg 1973) and points to thermal control for the base of the elastic layer.

When plotted as a function of lithospheric age, the estimates of effective elastic thickness (T_e) lie between the 300 and the 600°C isotherms (Fig. 1) according to the thermal plate model of Parsons & Sclater (1977). It is unlikely that this factor of 2 uncertainty in the temperature at the base of the elastic layer is caused solely by errors in the data. In this study we investigate to what extent the apparent variations in temperature can be attributed to the inadequacy of the purely elastic plate model for describing the mechanics of the oceanic lithosphere. For more physically realistic rheologies in which the elastic strength of the lithosphere is limited by brittle rock failure at shallow depths and ductile flow at the base, the observed T_e will be a function of both the curvature of the deformed plate and the magnitude and sign of axial loading forces.

Effect of yield strength on T_e

The homogeneous equation describing the bending of a plate subject only to mechanical equilibrium is

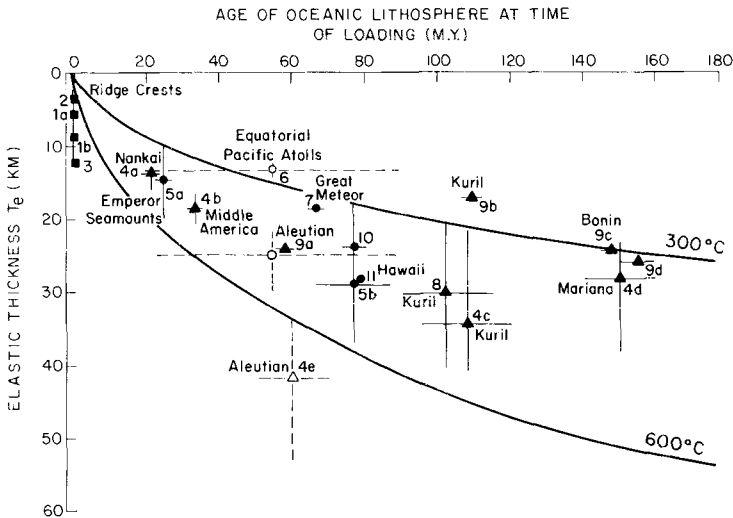$$d^2M/dx^2 - N \, d^2 w/dx^2 - \Delta\rho g w = 0 \tag{1}$$

Figure 1. Elastic thickness of the lithosphere versus age of the lithosphere at the time of loading. After Watts *et al.* (1980). Data sources: (1) Cochran (1979); (2) McNutt (1979); (3) McKenzie & Bowin (1976); (4) Caldwell (1979); (5) Watts (1978); (6) McNutt & Menard (1978); (7) Watts *et al.* (1975); (8) McAdoo *et al.* (1978); (9) Caldwell *et al.* (1976); (10) Suyenaga (1977); (11) Walcott (1970).

in which M is the bending moment, x is the horizontal coordinate, N is the axial load (+ for tension, − for compression), $\Delta\rho g$ is the buoyancy force arising from a density difference between fluids below and above the plate, and w is the plate deflection. Consistent with standard usage, w is positive upward, z is positive downward, and the restoring force $\Delta\rho g$ is positive for density increasing with depth. At any point x, the axial load can be obtained by integrating the stress differences $\Delta\sigma$ through a vertical cross-section of the plate with thickness H:

$$N = \int_0^H \Delta\sigma\, dz. \tag{2}$$

We assume that the horizontal and vertical stresses, σ_h and σ_v, are principal stresses so that $\Delta\sigma = \sigma_h - \sigma_v$. The moment is defined by the vertical integral of the fibre stresses σ_f weighted by the distance from the neutral plane of bending at a depth z_n:

$$M = \int_0^H \sigma_f (z - z_n)\, dz. \tag{3}$$

Since the fibre stresses must sum to zero over the thickness of the plate, in the absence of axial loading $\sigma_f = \Delta\sigma = \sigma_h - \sigma_v$.

Consider first the fibre stresses which develop in an elastic plate in pure bending, shown in Fig. 2(a). Stress differences $\Delta\sigma$ are linearly proportional to distance from the neutral axis
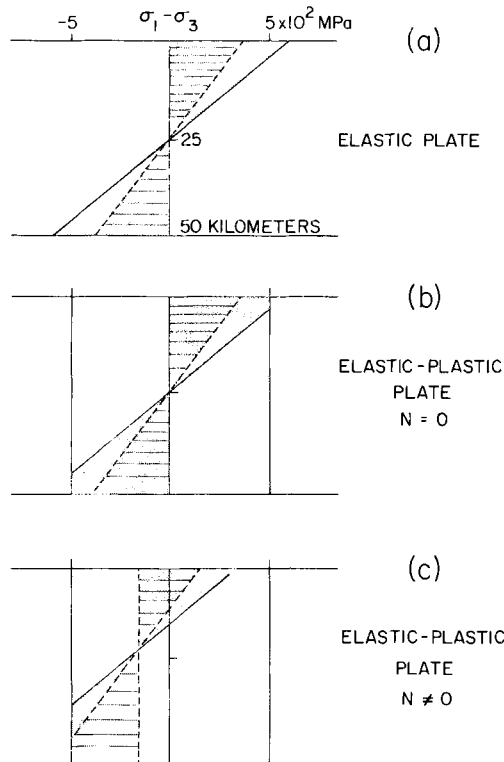

Figure 2. Stress differences versus depth within the bending lithosphere for low (horizontal lines) and high (shaded) plate curvature. (a) Elastic plate; (b) elastic-perfectly plastic plate; (c) elastic-perfectly plastic plate subjected to axial compression.

and reach maxima at the surface of the plate and at its base located at $z = T_e$. For a thin elastic plate,

$$M(x) = -DK(x) \tag{4}$$

where

$$D = E\,T_e^3/12(1 - \nu^2) = \text{the flexural rigidity,} \tag{5}$$

E = Young's modulus,

ν = Poisson's ratio,

$K = d^2 w/dx^2$ = the curvature of the plate.

For both the low and the high curvature cases shown in Fig. 2(a), we would find from equations (3)–(5) that the base of the plate H equals T_e.

There is no limit to the maximum stress differences allowed in a purely elastic plate. Since real Earth materials do have a finite strength, a more realistic stress difference profile is shown in Fig. 2(b) for an elastic-perfectly plastic rheology. The plate behaves elastically up to the yield stress $\Delta\sigma_0$, at which point the plate fails. Additional strain causes no increase in stress. When the plate has low curvature such that the maximum stress differences are everywhere less than the yield stress, there is no observational way to distinguish the elastic-plastic plate from the purely elastic one in Fig. 2(a). However, at higher curvatures the stress-difference profile in the elastic-plastic plate does differ from the elastic case because the uppermost and lowermost sections of the plate fail. Suppose we let

$H = 40\,\text{km}$,

$z_n = 20\,\text{km}$,

$K = -5 \times 10^{-7}\,\text{m}^{-1}$,

$\Delta\sigma_0 = 500\,\text{MPa}$,

and calculate the moment in the elastic-plastic plate using equation (3). According to equation (4), a purely elastic plate with the same moment and curvature would be less than 37 km thick. Thus a lithospheric plate which is more sharply bent will appear thinner than an identical plate with lower curvature if finite yield strength in not taken into account. In a similar manner, axial loading forces can cause an apparent plate thinning even for relatively low curvatures, as shown in Fig. 2(c).

The yield envelope

The elastic-perfectly plastic plate shown in Fig. 2(b) is useful for illustrative purposes but is simplistic in the sense that the yield strengh $\Delta\sigma_0$ in the oceanic lithosphere must be depth-dependent. A map of the yield strength in tension and compression as a function of depth in the lithosphere is called a yield envelope. The particular envelope that we adopt in this study is constrained by the results from experimental deformation of olivine and accounts for the effects of variations in pressure, temperature and strain rate on rock strength. Since the adaptation of olivine rheologies to lithospheric conditions and geological strain rates has been discussed in several recent publications (Mercier, Carter & Anderson 1977; Kirby 1977; Post 1977; Goetze & Evans 1979; Brace & Kohlstedt 1980; Kirby 1980), we only provide a brief discussion here.

Following Kirby (1980), we consider three regimes of rock behaviour: brittle, semi-brittle and ductile.

THE BRITTLE ZONE

In the uppermost, cool regions of the lithosphere, we assume that rocks fail by movement along localized fractures. Strength increases with overburden pressure but is relatively insensitive to temperature, strain rate and rock type. The shear stress τ necessary to overcome static friction on a surface with normal stress σ_n is (Byerlee 1968, 1978)

$$\tau = 80 + 600\,\sigma_n \text{ (MPa)}. \tag{6}$$

With a Mohr diagram, it can be shown easily that as differential stress increases, frictional sliding first occurs on faults oriented at about $30°$ to the largest compressional stress. Assuming that fracture surfaces with the proper $30°$ orientation are available, in terms of differential stress at first yielding, (6) becomes

$$\Delta\sigma_0 = -2.17\,\rho gz - 283 \text{ MPa} \qquad (\Delta\sigma < 0), \tag{7}$$

$$\Delta\sigma_0 = 0.68\,\rho gz + 89 \text{ MPa} \qquad (\Delta\sigma > 0) \tag{8}$$

in which ρgz is the overburden pressure in units of $10^{-6}\,\text{N m}^{-2}$. Use of (6) implies that the upper lithosphere is already fractured, and the validity of (7) and (8) depends on some of the fractures having the most favourable orientation for frictional sliding (Goetze & Evans 1979). In the absence of weakening effects from elevated pore-fluid pressures, (7) and (8) represent a lower bound on the yield stress in the top 20 km or so of the lithosphere. Note that the upper plate is significantly stronger in compression as compared to tension. Other factors being equal, a plate with negative curvature (concave downward) will appear to have a smaller T_e than a plate with positive curvature.

THE SEMI-BRITTLE ZONE

The transition between brittle and ductile behaviour is marked by a region in which both brittle and ductile processes occur. State of stress and temperature are both important environmental parameters, in that increasing pressure tends to inhibit stable microfracturing, and semi-brittle deformation halts at temperatures too low for plasticity in the specimen. Semi-brittle yielding is the principal mode of failure at intermediate depths where high pressure and low temperature would require stress differences exceeding 800–1000 MPa for either brittle or ductile deformation (Kirby 1980).

In this study, we do not include semi-brittle failure in formulating the yield envelope for the following reason. The observation that the neutral axis of bending occurs at mid-plate depths and the fact the regions of most intense curvature are concave downward conspire to render semi-brittle failure inconsequential to the bending lithosphere. In Fig. 3 we have superimposed the stress versus depth profile for the highest plate curvature considered in this study on to the yield envelope of Kirby (1980) modified for a strain rate or $10^{-16}\,\text{s}^{-1}$. No adjustment was made in Kirby's semi-brittle region based on the prediction that strain rate-independent brittle processes control semi-brittle behaviour (S. H. Kirby, private communication). The straight line through the neutral axis which represents the magnitude of elastic fibre stresses intersects the yield envelope at approximately 27 km depth in extension, which is too shallow for semi-brittle behaviour. In compression, semi-brittle deformation occurs at lower pressures corresponding to depths less than 20 km and could be an important weakening mechanism directly under seamounts where the upper lithosphere is under relative compression.

The elastic portion of the stress curve intersects the lower boundary of the yield envelope just below the region referred to by Kirby (1980) as 'ductile-low temperature', a process
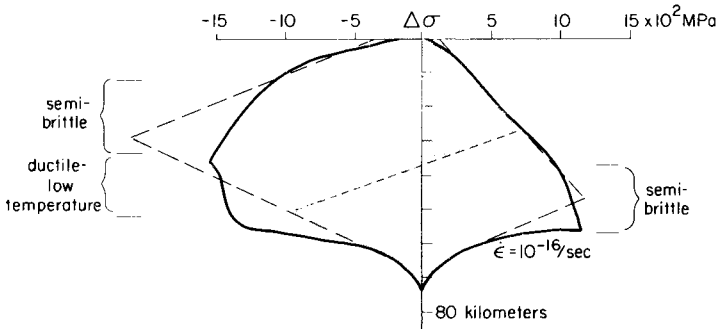
Figure 3. Yield envelope showing strength versus depth within the lithosphere for a brittle/elastic/ductile rheology. Solid curve: model proposed by Kirby (1980) modified for a strain rate of $10^{-16}\,\mathrm{s}^{-1}$. Dashed curve: simplified form of yield envelope adopted in this study, generated assuming the same activation energy, temperature structure and strain rate as in Kirby's model. Shaded region shows stress differences versus depth for a plate with large curvature.

controlled by intercrystalline glide. According to Fig. 3, this deformation mechanism will not enter into this study, nor will it be observed for plate curvatures of the opposite sign. Trenchward of the first zero crossing most flexure profiles displace curvatures larger than those considered here, and it is in this region that ductile-low temperature flow may be important.

THE DUCTILE ZONE

At higher temperatures, the dominant mechanism for failure is ductile flow. Yield strength is fairly insensitive to pressure effects but decreases with decreasing strain rate. The transition from high strength ($> 1000\,\mathrm{MPa}$) to low strength ($< 10\,\mathrm{MPa}$) occurs over a limited depth range due to the extreme temperature sensitivity of the process, hence giving rise to plate-like behaviour.

For the range of $\Delta\sigma < 200\,\mathrm{MPa}$, we adopt a power-law relationship between yield strength $\Delta\sigma_0$ and strain rate $\dot{\epsilon}$ (Goetze 1978; Evans & Goetze 1979):

$$\Delta\sigma_0 = [\dot{\epsilon}/B_1 \exp(Q_L/RT)]^{1/n} \tag{9}$$

in which

$B_1 = 7.0 \times 10^{-14}\,\mathrm{s}^{-1}\,\mathrm{Pa}^{-n}$,

Q_L = the activation energy,

$R = 1.987 \times 10^{-3}\,\mathrm{kcal}\,(\mathrm{mol}\,\mathrm{K})^{-1}$,

T = temperature in degrees Kelvin,

$n \approx 3$.

For $\Delta\sigma > 200\,\mathrm{MPa}$,

$$\Delta\sigma_0 = \sigma_H \{1 - [RT/Q_H \ln(B_2/\dot{\epsilon})]^{1/2}\} \tag{10}$$

in which

$\sigma_H = 8.5 \times 10^9\,\mathrm{Pa}$,

Q_H is slightly larger than Q_L to ensure continuity at $\Delta\sigma = 200\,\mathrm{MPa}$,

$B_2 = 5.7 \times 10^{11}\,\mathrm{s}^{-1}$.

To account for the well-accepted age-dependence of the thermal structure in the oceanic lithosphere, we assume that the temperature is related to depth via a linear gradient which decreases as the square root of age, t:

$$T(t, z) = T_0 + \alpha/\sqrt{t}\, z \qquad (11)$$

where T_0 has units K and α is the temperature gradient in $K\sqrt{Myr}\ km^{-1}$.

The strain rate sensitivity of (9) and (10) requires that $\dot{\epsilon}$ be known only to within an order of magnitude. The specification of the activation energy Q and the temperature T is critical; Q/RT should be accurate to within 10 per cent, but is not known at present to that precision. Without specifying the exact values for Q and T, we can see from (9) that the base of the mechanical lithosphere, defined here as the depth at which the yield strength at geological strain rates is less than 50 MPa, corresponds to $Q/RT = 60$. In this study, we use actual observations of lithospheric deflection to constrain the depth, as a function of lithospheric age, at which Q/RT falls to 60.

The moment-curvature formulation

The most straightforward, but time-consuming, method of fitting observed flexure profiles using non-elastic rheologies is to integrate equation (1) from large x in towards the flexed region. At each step, the moment for a given rheology is calculated from equation (3) and transformed into an effective flexural rigidity D_{eff} by equation (4). D_{eff} varies as the curvature changes along the profile. The yield envelope which determines the stresses in (3) can be adjusted until the deflection w agrees with the data (McAdoo, Caldwell & Turcotte 1978; Bodine & Watts 1979; Bodine, Steckler & Watts 1981).

When the object of the investigation is simultaneously to consider the rheological implications of numerous flexure profiles, the problems can be quickly parameterized using an extension of the method of Goetze & Evans (1979). Integrating equation (1) twice yields

$$M(x_0) = \int_{x_0}^{\infty} \Delta\rho g w(x)\,(x - x_0)\,dx + N\,w(x_0) \qquad (12)$$

which measures the moment at a point x_0 regardless of rheological assumptions. Physically, (12) sums up the torques about x_0 caused by the weight of the deformed plate and the axial load, as illustrated in Fig. 4. While (12) is a rheologically independent measure of the moment at x_0, the equal-but-opposite moment $M(x_0)$ in (3), arising from fibre stresses in the plate, is extremely dependent on rheology, in particular, on the depth H at which stress differences become insignificant. By equating the moments from equations (12) and (3), we can use deflection profiles w to constrain the stress differences in a vertical cross-section of the lithosphere at the point x_0.

Ideally, we want (12) to depend only on observable quantities, with no assumptions. For this reason, the optimal choice for x_0 in parameterizing trench profiles is the first zero crossing seaward of the trench axis. To begin with, because $w(x_0) = 0$, even if axial loading N is appreciable, it will not be a factor in equation (12). Only observed quantities, either the bathymetric profile w or the free air gravity anomaly $\Delta\rho g w$, directly determine $M(x_0)$, and this measure of the moment is insensitive to small errors in w. In addition, in order to calculate $M(x_0)$ in (3), we must specify the curvature K at x_0, which then determines the stress differences in the non-yielded portion of the lithosphere. While the integration in (12) may be quite stable, the second derivative of w, the curvature, is notoriously unstable. Fig. 5 shows some examples of this effect: small changes in the bathymetric curve cause very large changes in curvature. In the example from Liu (1980), the difference in deflection for an
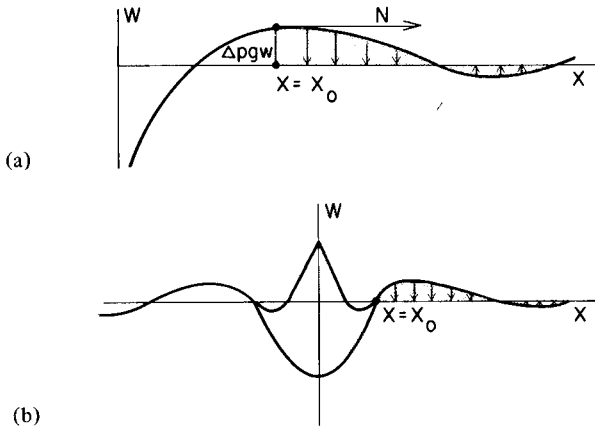
Figure 4. Illustration of physical basis for calculation of observed moments from flexed lithosphere. Shading shows area over which moment integral is performed. (a) Subduction zone case for arbitrary x_0. In this study, x_0 is chosen to lie at the first zero crossing so that $Nw(x_0) = 0$. (b) Seamount loading case.
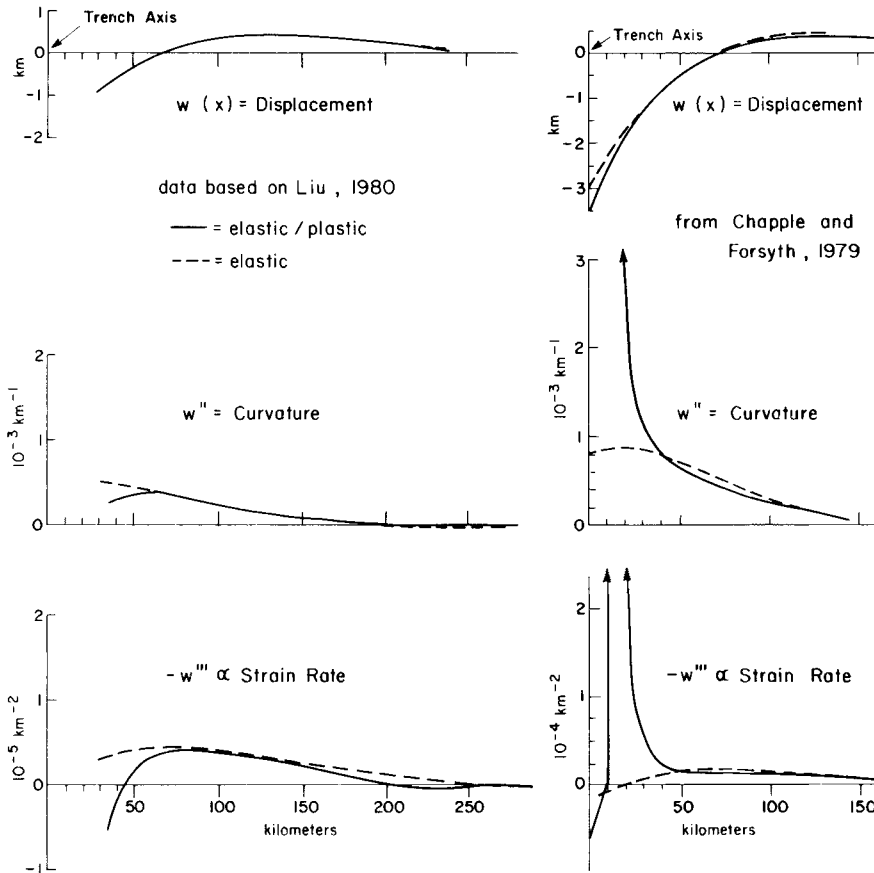

Figure 5. Comparison of deflection, curvature and strain rate for elastic and elastic/plastic models of plate flexure at subduction zones proposed by Liu (1980) and Chapple & Forsyth (1979). Close agreement on plate deflection for elastic and elastic/plastic models does not ensure agreement on curvature and strain rate, particularly landward of the first zero crossing.

elastic plate compared to his model for an elastic/plastic plate is less than the width of the line, but curvature on the outer trench wall varies by a factor of 2. The discrepancy in curvature estimates is more drastic in Chapple & Forsyth's (1979) study, but the similarity between w-profiles for elastic and elastic/plastic models was not impressive to begin with. Note, however, that in both studies the two plate models essentially agree on the curvature estimate at the first zero crossing seaward of the trench axis.

Likewise for flexure profiles caused by the loading of islands and seamounts, the optimal x_0 corresponds to the first zero crossing seaward of the load (Fig. 4b). Although axial forces N may not be as important in the seamount case, we still require a reliable estimate for K. More importantly, inboard of the first zero crossing, sediments, volcanic flows and the load itself add additional moments and obscure the flexure profile, violating the requirement that w be an observed quantity.

Parameterizing the data

The moment integral (12) becomes unstable at large values for $(x - x_0)$ if there is noise in the bathymetric or gravity profile. In this paper, 'noise' is defined as any features unrelated to plate flexure. Smoothing the data with an analytical curve removes this problem, and as far as (12) is concerned, the choice of curve is immaterial as long as it fits the data. The curvature estimate is, however, sensitive to the choice of analytical function because, as we discussed earlier, displacements which appear arbitrarily close can correspond to vastly different curvatures. The observation that the deformation of old oceanic lithosphere appears to be at least partly elastic suggests that the curvature estimate from the solution for bending a thin elastic beam may not be too much in error:

$$w(x) = A \exp(-x/\alpha) \sin(x/\alpha). \tag{13}$$

The wavelength α and the amplitude A of this damped sinusoid are chosen so that (13) provides a best fit to the data in the least squares sense.

Caldwell *et al.* (1976) show that A and α are related to the height w_b of the outer rise seaward of a subduction zone and the distance x_b from the first zero crossing to w_b by

$$w_b = A \exp(-\pi/4)/\sqrt{2},$$

$$x_b = \pi\alpha/4.$$

The point x_0 where we have chosen to calculate the moments corresponds to $x = 0$ in the notation of (13). In terms of w_b and x_b, the moment M and curvature K are:

$$M(x = 0) = \int_0^\infty \Delta\rho g w(x) \, x \, dx = \Delta\rho g w_b (4x_b/\pi)^2 \exp(\pi/4)/\sqrt{2},$$

$$K(x = 0) = d^2 w/dx^2 = -\sqrt{2}\pi^2 \, w_b \exp(\pi/4)/8x_b^2.$$

The strain rate averaged over the thickness of the plate H is

$$\dot\epsilon = \frac{d}{dt} (H/4 \, d^2 w/dx^2).$$

Assuming that the flexure profile is steady state,

$$\frac{d}{dt} = \frac{d}{dx} \cdot \frac{dx}{dt} = v \frac{d}{dx}$$

$$\dot\epsilon = Hv/4 \, d^3 w/dx^3$$

$$= \sqrt{2}(\pi/x_b)^{5/3} \exp(\pi/4) \, v \, w_b \, \{12 \Delta\rho g(1 - v^2)/E\}^{1/3}/32$$

14

Table 1. Assumed values for physical parameters.

$\Delta\rho$ = (asthenosphere—water) density = 2300 kg m^{-3}
g = 9.8 m s^{-2}
ν = 0.25
E = 8 $\times$ 10^{10} N m^{-2}

in which v is the plate velocity normal to the subduction zone. When w_b is expressed in m, x_b in km, and v in mm yr^{-1}, the above equations become:

$$M(0) = 5.67 \times 10^{10} \, w_b \, x_b^2 \, (\text{N}), \tag{14}$$

$$K(0) = -3.83 \times 10^{-6} \, w_b / x_b^2 \, (\text{m}^{-1}), \tag{15}$$

$$\dot{\epsilon}(0) = 3.07 \times 10^{-18} \, v \, w_b \, x_b^{-5/3} \, (\text{s}^{-1}) \tag{16}$$

using the parameters in Table 1.

A similar parameterization exists for the moment at the first zero crossing seaward of seamount loads:

$$M = C_1 \, w_b \, x_b^2, \tag{17}$$

$$K = C_2 \, w_b / x_b^2 \tag{18}$$

in which the values for C_1 and C_2 depend upon the geometry. For a chain of seamounts that approximate a line load, C_1 and C_2 are identical to the values in (14) and (15) regardless of whether the plate is continuous or fractured beneath the load. For an isolated seamount with circular geometry,

$$C_1 = 9.06 \times 10^{10}, \tag{19}$$

$$C_2 = -2.58 \times 10^{-6}. \tag{20}$$

The derivation of these values is given in Appendix A, along with a brief demonstration of the observations that:

(1) for a given flexural rigidity D and density contrast $\Delta\rho$, x_b and the wavelength of the bulge are virtually independent of the details in loading geometry landward of the first zero crossing;

(2) for a constant load volume, w_b (and M) decrease as the load radius increases;

(3) the reduction in moment compared to the point load approximation becomes appreciable when the radius of the load approaches $(D/\Delta\rho g)^{1/4}$.

We see from (14), (15), (17) and (18) that estimates of w_b and x_b should directly yield estimates of moment and curvature at the first zero crossing. While trench profiles are commonly parameterized in terms of these two quantities, corresponding values are hardly ever reported for seamount profiles. Because the total strain beneath seamounts is an order of magnitude less than trench deformations, their peripheral bulges tend to be lower in amplitude and more diffuse than outer rises seaward of trenches, making it difficult to accurately estimate x_b and w_b. As shown in Appendix A, knowledge of the load P, its distribution and the flexural rigidity D can be converted into estimates of x_b and w_b, except for the unfortunate fact that most attempts to determine D have not actually dealt with the total load, equal to the sum of the volcano, its root, the archipelagic apron and any sediments in the moat. As pointed out in McNutt & Menard (1979), for a given x_b, the artifice of including the unknown root and moat material in the buoyancy term with $\Delta\rho$ = (3300—2800) kg m^{-3}

results in an underestimate of D by a factor of approximately 50 per cent and a ~ 40 per cent overestimate of w_b when compared to the more realistic treatment in which all root and moat material are placed in the loading term P and the $\Delta\rho$ over the rise equals $(3300-1000)\,\text{kg m}^{-3}$. Therefore, we shall confine the seamount data set to include only examples in which w_b and x_b are reasonably well constrained.

The strain rate estimate for seamount flexure is fundamentally different from that of trenches. In (16) we assume that the outer rise is steady and fixed with respect to the trench axis. A given plate element experiences strain as it travels up the outer rise and down into the trench, with strain rate proportional to plate velocity and change in curvature. For the seamount case we assume that the flexure is fixed with respect to the plate and that the strain rate is proportional to the loading rate. The second assumption is valid if the load's growth through dyke injection and upward transport of magma is fairly steady state and occurs over a time span longer than the relaxation of the lower lithosphere (several tens of thousands of years).

The loading rate $\dot{V}$ for a volcano, equal to (volume)/(duration of activity) is difficult to estimate because the age of the rocks in the root beneath the volcano is poorly known. For a feature such as Hawaii, the duration of volcanism must be greater than the age of the oldest dated rocks on Kohala Mountain, 0.68 Myr (Dalrymple 1971). Assuming that 1.5 Myr is a reasonable estimate for the total duration of activity and using the volume estimate for Hawaii given in Appendix B, we find that

$$\dot{V} = (2.08 \times 10^{14}\,\text{m}^3)/(1.5 \times 10^6\,\text{yr})$$
$$= 1.4 \times 10^8\,\text{m}^3\,\text{yr}^{-1} = 4.4\,\text{m}^3\,\text{s}^{-1}.$$

This estimate is only slightly larger than the $10^8\,\text{m}^3\,\text{yr}^{-1}$ calculated by Swanson (1972) from recent eruptions on Kilauea and probably represents an approximate sum of contributions from intrusive as well as extrusive volcanism. We will assume that other oceanic islands have loaded the lithosphere at a similar rate.

We can now estimate the strain rate using

$$\dot{\epsilon} = \frac{H}{4}\,\frac{d}{dt}\,(d^2 w/dx^2) = \frac{H}{4}\,C_2\,\dot{w}_b/x_b^2$$

assuming that the position of the bulge remains fairly constant while its amplitude increases from mass additions. In terms of w_b and x_b,

$$\dot{\epsilon} = 3.03 \times 10^{-18} x_b^{-2/3} w_b. \tag{21}$$

Equation (21) is theoretically valid only during the period of constant growth of the load. When volcanism ceases the strain rate is then controlled by the slow thinning of the plate from below by long-term creep under a constant surface load (Bodine *et al.* 1981). Studies have shown, however, that the apparent rigidity of the lithosphere along the Hawaiian chain does not decrease with the age of the load (Watts & Cochran 1974; Watts 1978). We will therefore assume that the slow thinning of the plate after cessation of volcanism is not resolvable for relatively recent loads whether active or not and that (21) still applies.

Equations (14)–(21) provide a simple parameterization of flexure profiles in terms of observed quantities. With the calculated curvatures and strain rates, the observed moments can then be compared to theoretical moments from various yield envelopes which include brittle and ductile, as well as elastic, behaviour. The translation of w_b and x_b into M, K

and $\dot{\epsilon}$ by means of the elastic plate equation is valid only to the extent to which changes in moment as a function of temperature structure, curvature and strain rate appear as variations in effective elastic thickness T_e.

The data

For a suite of flexure profiles caused by either plate subduction or seamount loading we calculated moment, curvature and strain rate using equations (14)–(21). We selected only profiles for which w_b and x_b can be observed, the age of the lithosphere is known (Sclater, Parsons & Jaupart 1981), and (in the case of trenches) the plate velocity is reasonably well contrained. The data are summarized in Tables 2 and 3. The underlined values from Caldwell *et al.* (1976) are considered the most reliable because the profiles were corrected for variations in sedimentation and age along the profile prior to fitting an equation of the form (13) to the data. For situations in which the same profile was modelled in separate studies, the amplitude and wavelength data from the sediment- or age-corrected profile is reported. The Aleutian Seamap 13-4 profile was the only case in which such corrections produced a significant difference in the moment and curvature, and in general separate investigators agreed on the values of w_b and x_b for any given track line.

Reliable moment/curvature estimates are more difficult to obtain for the seamount examples due to the frequent association of off-ridge volcanism with midplate swells. For example, the moat and arch caused by the load of the Hawaiian ridge is superimposed on a longer wavelength swell (Hamilton 1957) that distorts both the amplitude and wavelength of the arch. The observed values for x_b and w_b may not be the appropriate input for (17) and (18). The more successful studies of Hawaiian flexure have dealt with free air gravity anomalies rather than bathymetry (Watts & Cochran 1974; Watts 1978). The value for the flexural rigidity D is found such that the plate is stiff enough to explain the large-amplitude anomalies over the ridge. This technique leads to plate parameters which systematically underestimate the amplitude of the gravity anomaly over the arch (Watts & Cochran 1974), and in general it is impossible to explain the height of the bulge which exceeds 300 m on some profiles within the context of a simple plate-flexure model using any reasonable density for the Hawaiian ridge. The Great Meteor seamount may rest upon a less obvious swell in that, again, the best-fitting plate parameters seriously underestimate the amplitude of the free-air anomaly over the peripheral arch (Watts, Cochran & Selzer 1975, fig. 6).

Table 3 summarizes the seamount data for the three cases with well-documented lithospheric flexure. Values for x_b are the observed distances from the nodal point to the crest of the arch in the topography or gravity but are uncertain to the extent that long-wavelength swells distort the flexure. The amplitudes w_b for Hawaii and the Great Meteor seamount represent a guess as to the contribution to the arch from seamount loading alone. For Rarotonga, both x_b and w_b are 'observed' quantities deduced from the distribution and amplitude of uplifted atolls in the vicinity of the active volcano. If erosion of the uplifted atolls is unimportant, there appears to be no discrepancy between observed arch amplitude and estimated amplitude from flexure alone (McNutt & Menard 1978).

Results

The moment/curvature information from the data in Table 2 for old oceanic lithosphere is plotted in Fig. 6. An obvious feature from the data points is that there is little distinction between observations from 100 and 165 Myr old lithosphere (points 1–11). If the oceanic lithosphere were to continue cooling and thickening at ages beyond 100 Myr, we would expect to see higher moments (corresponding to a thicker plate) for the very oldest

Table 2. Trench profiles.

No.	Location	Profile	Age (Myr)	Velocity (mm yr⁻¹)	Strain rate ×10⁻¹⁶ s⁻¹	W_b m	x_b km	Curvature ×10⁻⁷ m⁻¹	Moment ×10¹⁶ N	Source
1	Marianas	Scan 5	>165	73	1.4	500	55	6.3	8.6	Caldwell et al. (1976)
2	Marianas		>165	73	1.2	550	63	5.4	12	Carey & Dubois (1981)
3	Bonin	Bent 2–2	130	87	2.1	640	55	8.0	11	Jones et al. (1978)
4	Bonin	Japanyon 4	130	87	1.5	820	78	5.1	29	Jones et al. (1978)
5	Bonin	Hunt 1–4	130	87	1.6	570	59	6.3	11	Jones et al. (1978)
6	Bonin	Bent 1–3	130	87	1.6	420	49	6.5	5.8	Jones et al. (1978)
7	Bonin	Antipode 3	130	87	1.9	350	40	8.2	3.3	Jones et al. (1978)
8	Bonin	Hunt 3 Aries 7	130	87	1.4	400	53	5.5	6.4	Caldwell et al. (1976)
9	Japan	Bent 1–1	130	87	0.6	620	115	1.8	47	Jones et al. (1978)
10	Kuril	Zetes 2	100	83	1.4	280	42	6.1	2.8	Caldwell et al. (1976)
11	Kermadec	Geo 318	100	83	0.5	240	71	1.8	6.9	Carey & Dubois (1981)
12	Aleutian	Seamap 13–4	55	72	1.0	350	53	4.8	5.6	Caldwell et al. (1976)
13	Middle America	Iguana 4–2	20	84	0.8	129	36	3.9	0.92	Jones et al. (1978)
14	Middle America	Iguana 2	20	84	0.8	106	34	3.5	0.70	Jones et al. (1978)

Table 3. Island and seamount data.

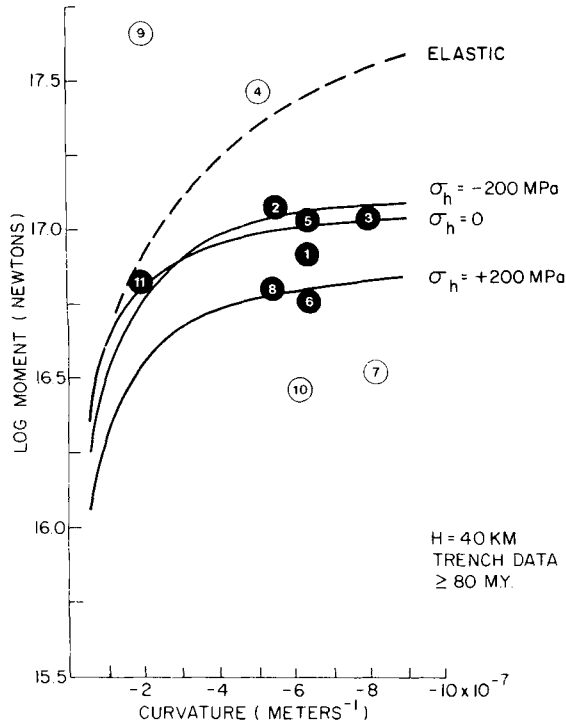| No.	Location	Age of crust (Myr)	Age of load (Myr)	Strain rate ×10⁻¹⁶ s⁻¹	w_b (m)	x_b (km)	Curvature ×10⁻⁷ m⁻¹	Moment ×10¹⁶ N	Source
15	Hawaii	80	Less than 1	0.15	55	60	0.4	1.8	Hamilton (1957) Watts (1978)
16	Great Meteor	81	15	0.07	30	45	0.4	0.55	Watts et al. (1975)
17	Ratotonga	70	1–2	0.40	50	40	0.8	0.72	McNutt & Menard (1978)

Figure 6. Plot of log (moment) versus curvature at the first zero crossing for trench flexure profiles on crust older than 100 Myr. Numbers correspond to entries in Table 2. Filled-in circles are considered the most reliable. Smooth curves are theoretical moment/curvature relationships from a yield envelope with the form of Fig. 7.

examples. These data, therefore, support the plate model as opposed to a boundary layer model for thermal evolution of the oceanic lithosphere.

For curvatures of the order of $7 \times 10^{-7}\,\mathrm{m^{-1}}$, the yield envelope shown in Fig. 3 produces a moment of $4 \times 10^{17}\,\mathrm{N}$, which is clearly too large to explain most of the data in Fig. 6. The two most obvious means of weakening the lithosphere to the point of agreeing with the data are:

(a) decreasing the depth of the base of the yield envelope by increasing the geothermal gradient or reducing Q;

(b) increasing the slope of the yield envelope in the brittle zone by invoking elevated pore-fluid pressure to offset the increase in strength with increasing overburden pressure.

The solid curves in Fig. 6 show theoretical moment/curvature relations corresponding to the first tactic, moving the base of the yield envelope in Fig. 3 from 70 to 40 km depth, as shown in Fig. 7. By postulating modest $+200\,\mathrm{MPa}$ axial loading forces (Fig. 7), the theoretical curves encompass seven out of 11 of the data points. The uncertainty in the data, however, would preclude making any definite statements about the sign of the horizontal thrust at any particular trench.

All four data points (4, 7, 9, 10) which lie beyond the $+200\,\mathrm{MPa}$ bounds correspond to ship tracks which sample the trench and outer rise near the intersection of different trench systems (Fig. 8), and all except profile 10 from the Kuril trench require projection of the data through a large angle to produce a profile normal to the trench axis. Since trench systems are arcuate rather than linear, the projection operation is not strictly valid.
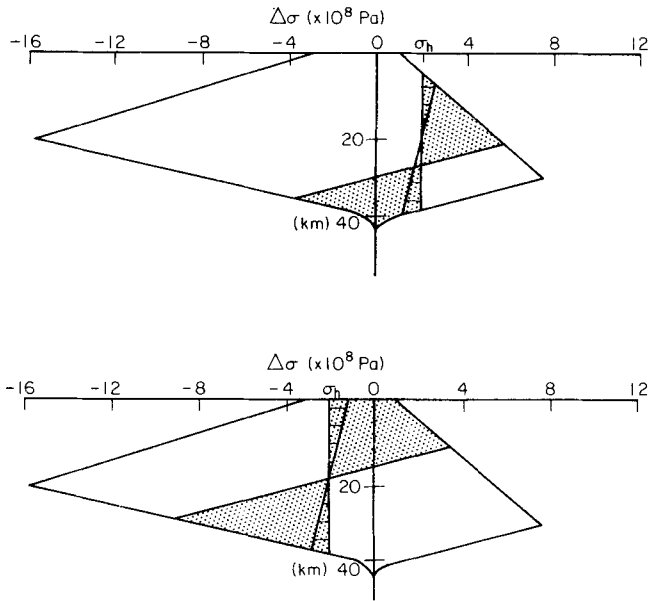
Figure 7. Yield envelope for the 100 Myr old curve in Fig. 8. Stress differences are given as a function of depth for lithosphere subjected to axial loading. Region with horizontal striping show $\Delta\sigma$ versus depth for plate curvature 0.5×10^{-7} m^{-1}. Shaded region is $\Delta\sigma$ versus depth for a curvature of 9×10^{-7} m^{-1}.
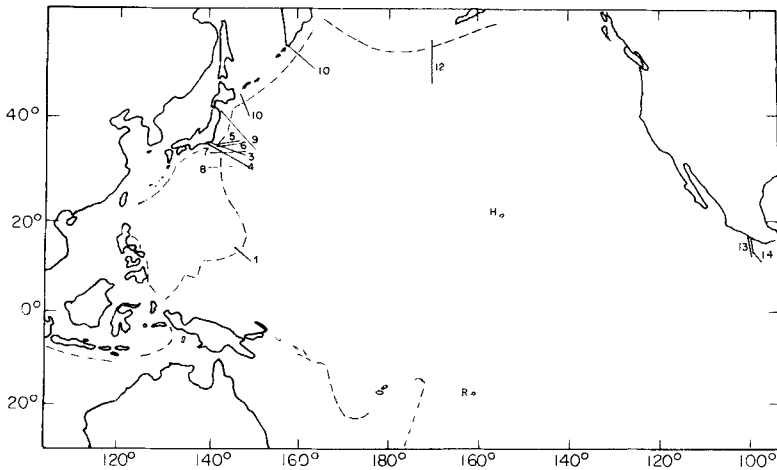

Figure 8. Index map of the Pacific Ocean showing the location of the ship tracks listed in Table 2. H corresponds to Hawaii and R to Rarotonga. Dashed lines give location of trench axis. Modified from Jones *et al.* (1978).

Especially for large projection angles, the estimates of x_b and w_b will not correspond to the same trench cross-section and maybe not even to the same trench. A glaring example of this problem is illustrated by the intersecting profiles 4 and 7 from the Bonin trench (Fig. 8), which indicate anomalously large and small moments, respectively. If the trench system were linear, after projection the two profiles should have been identical, which is clearly not the case. It makes more sense to assume that either the x_bs or the w_bs should be exchanged for profiles 4 and 7, thereby producing moment/curvature estimates clustering with the other Bonin values.

Although breakdown of the linearity assumption is an unlikely error source for the Kuril profiles, other investigators have also suggested that subduction at this trench might be anomalous. Using the same data, Goetze & Evans (1979) proposed that the Kuril lithosphere either has an abnormally warm geotherm or is subjected to tensile stresses in excess of 100 MPa. Our estimate from this study is that either the thermal gradient is equivalent to that of 40 Myr old lithosphere or horizontal tension exceeds 200 MPa. However, the Zetes 2 profiles are not representative of the Kuril system as a whole. In a very thorough analysis of 10 profiles sampling the entire length of the Kuril system, McAdoo et al. (1978) conclude that axial compressive loads vary between 250 and 500 MPa, plate thickness varies from 25 to 47 km, and yield stress varies from 500 to 720 MPa within the context of an elastic-perfectly plastic plate model such as in Fig. 2 (b and c). Even if the data were interpreted in terms of the yield envelope used here, we would have to postulate rapid, factor 2 fluctuations in some combination of parameters such as geothermal gradient, axial loading forces, Q values and pore pressure. Such variability is not required along other trench systems. For example, Bodine & Watts (1979) find that 25 profiles along the Izu-Bonin and Mariana trenches do not require variations in H or in the yield criteria but can be explained by modest (±100 MPa) changes in axial loading. Clearly the Kuril trench is more complicated than our simple models. The possibility also exists that plate structures unrelated to bending confuse the analysis.

Since profiles 4, 7, 9 and 10 appear to be poorly suited for an analysis of flexure, we will exclude them from the remainder of the discussion. As shown in Fig. 6, the moment/curvature estimates corresponding to these ship tracks are either unreliable or unrepresen-
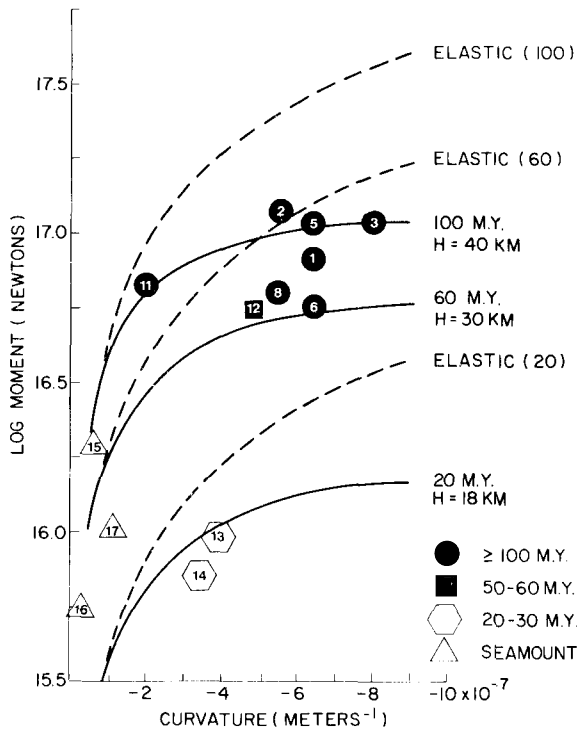

Figure 9. Fit between moment/curvature data and predictions from preferred yield envelope in which the base of the mechanical lithosphere is constrained to lie at 40 km depth for 100 Myr old lithosphere and vary as the square root of age for younger lithosphere. Dashed curves are theoretical relations for purely elastic plates with the same plate thickness ($T_e = H$).

tative, and furthermore are not predicted by the elastic plate (dashed curve), brittle/elastic/ductile model (solid curves), or any other simple rheology.

From Fig. 6 we conclude that it is possible to satisfy the moment/curvature information from old oceanic lithosphere by supposing that $Q/RT = 60$ at 40 km depth for 100 Myr old lithosphere. Combined with equation (11), this result implies that $H/\sqrt{t}$ = a constant = 4 for H in km and t in Myr. Therefore, at $t = 20$ Myr, $H \approx 18$ km and at $t = 60$ Myr, $H \approx 30$ km. In Fig. 9 we show that the moment/curvature relations from the yield envelope model with its base at these depths does give a reasonable fit to the data from younger lithosphere.

Three seamount examples are included in Fig. 9 for comparison with the trench data, but for several reasons we will not weight the data too strongly. To begin with, the curvature at the first zero crossing seaward of the load is small compared to the examples from trench profiles, and falls in a region in which small errors in curvature cause very large changes in the rheological plate model. Secondly, the seamount data must be plotted without reference to lithospheric age, since the associated swells are good evidence for thermal rejuvenation (Detrick & Crough 1978). Although this reheating is probably confined to the lower lithosphere, it causes a small, but observable, reduction in the elastic plate thickness relative to normal oceanic lithosphere of similar age (Menard & McNutt 1982). Finally, a more representative strain rate for the seamount examples would be a factor of 10 less than the 10^{-16} s^{-1} used in calculating the theoretical curves in Fig. 9. However, the lower strain rate would only result in a 2—3 km reduction in H.
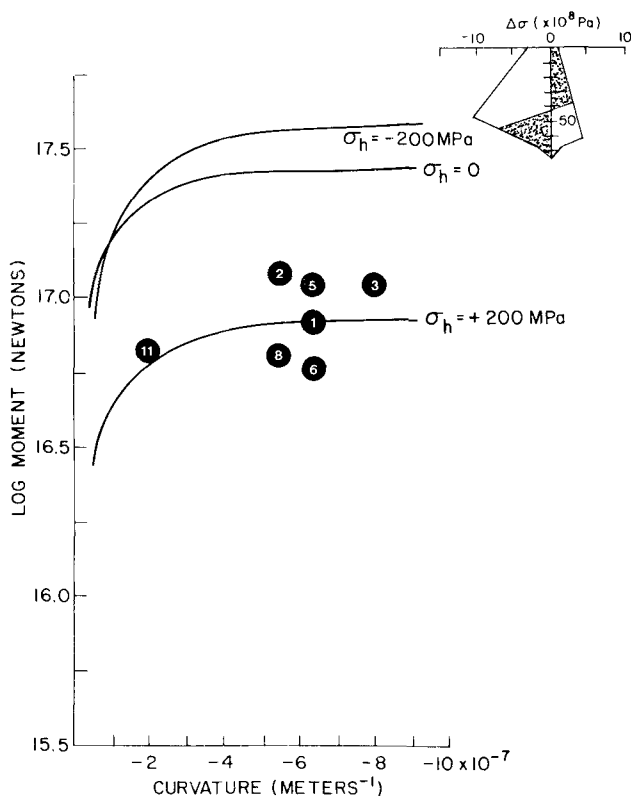

Figure 10. Same as Fig. 6 except that in computing the theoretical curves the brittle portion of the plate is assumed to have pore pressure equal to 0.7 times the lithostatic pressure (see inset of yield envelope for $\sigma_h = 0$ case).

While it is possible to explain the moment/curvature data by modifying the depth to the base of the laboratory yield envelope in Fig. 3, we must investigate whether the same result might be achieved through pore-fluid effects in the brittle zone without shoaling the high strength/low strength transition. Suppose we let $\lambda = $ (pore pressure)$/\rho g z$, and take the extreme case in which $\lambda = 0.7$ (Brace & Kohlstedt 1980). The effective overburden pressure is then $\rho g z (1 - \lambda)$, so that the strength increase with depth is not nearly so rapid. The resulting yield envelope and moment/curvature relations for old oceanic lithosphere are shown in Fig. 10. Even for this extreme case, the elevated pore pressure has not sufficiently reduced the moments, so that all trenches would appear to be in relative tension. The fit is even worse for crust of younger age, as shown in Fig. 11, assuming that $H/\sqrt{t} = 7$. Elevated pore fluid pressure is a less efficient way of reducing the moment simply because the greatest contribution to M comes from stress differences at large $(z-z_n)$. In the upper lithosphere the stress difference at the maximum $(z-z_n)$ is small regardless of pore pressure. In addition, this model predicts that the neutral axis of bending for 100 Myr old lithosphere lies below 40 km, which is inconsistent with the compressional focal mechanisms at 40 km reported by Chapple & Forsyth (1979).

We conclude that elevated pore pressure cannot be the primary weakening mechanism that brings the laboratory-derived yield envelope (Fig. 3) into agreement with the flexure data. The high strength/low strenth transition must occur at depths less than 70 km in old
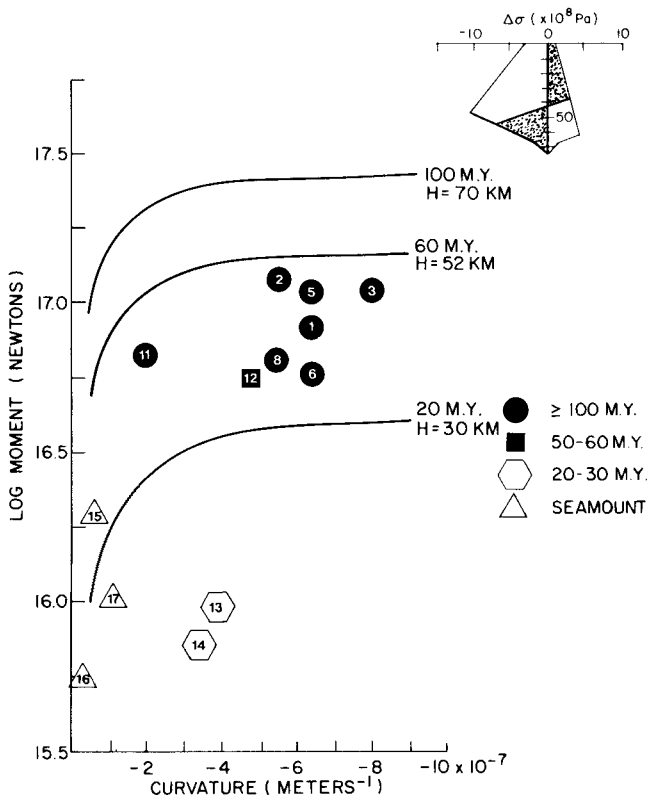

Figure 11. Comparison between moment/curvature data and predictions from yield envelope with pore pressure equal to 0.7 times lithostatic pressure for several different ages of crust. The base of the mechanical lithosphere is constrained to lie at 70 km depth for old oceanic lithosphere.

oceanic lithosphere, but our estimate of 40 km may be too shallow if pore-fluid pressure is significantly above hydrostatic.

Several points are worth noting in Figs 6 and 9. To begin with, the data show the clear saturation of moment at high curvature, as predicted by models with finite yield strength. Secondly, the brittle/elastic/ductile model is more successful in explaining variations in observed moment at subduction zones because it is sensitive to axial loading forces. The purely elastic model, shown by the dashed line in Fig. 6, predicts that the moment/curvature relation is independent of N. Regional tension is more effective than regional compression in explaining variations in moment. This result is a consequence of the smaller $d\sigma/dz$ slope of the brittle failure envelope for relative tension. Finally, within the limitations of this sort of analysis, the flexure of the seafloor surrounding seamounts provides virtually no information on yield strength, because the moment/curvature estimate falls in a region where the purely elastic plate is indistinguishable from the model with brittle and ductile failure.

Discussion

From the results in Figs 6 and 9 we conclude that $Q/RT = 60$ occurs at approximately 40 km depth for 100 Myr old lithosphere and at 18 km for 20 Myr old lithosphere. The activation energy Q is then related to temperature parameters T_0 and α by

$$Q = 0.119(T_0 + 4\alpha)$$

for Q in kcal mol^{-1}, T_0 in K and α in K(km$\sqrt{}$Myr)$^{-1}$. It is customary to let $T_0 = 273$ K so that a linear geotherm intersects the plate surface at 0°C. Other values for T_0 would account for a non-linear geotherm in the uppermost lithosphere without changing the rest of the analysis. In Fig. 12 we plot Q versus α for two common choices for T_0. The horizontal scale is $\alpha/10$ so that the numbers correspond to the thermal gradient for 100 Myr old lithosphere. Also shown are estimates of the geotherm for old oceanic crust from thermal plate models of Sclater & Francheteau (1970) and Parsons & Sclater (1977). The pyroxene geotherm of
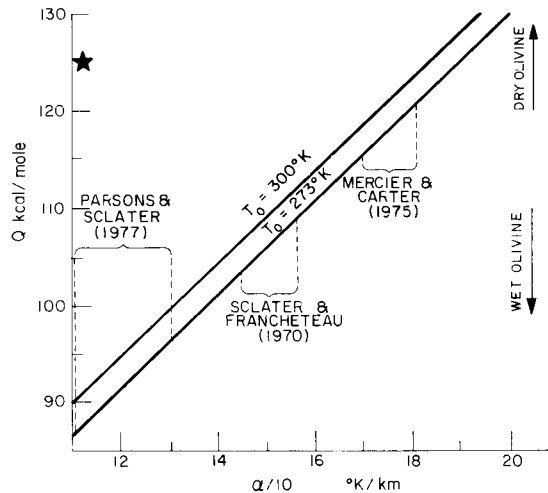

Figure 12. Trade-off curves between activation energy Q and temperature gradient for 100 Myr old lithosphere $\alpha/10$ for two choices of the temperature intercept T_0. Star indicates the values for Q and $\alpha/10$ used to generate the yield envelope in Fig. 3. Brackets show estimates of the temperature gradient in old oceanic lithosphere from several studies.

Mercier & Carter (1975), shown for comparison, represents an upper bound on the normal thermal gradient because the samples consist of lherzolite xenoliths from Kauai, formed by the Hawaiian hot spot. The thermal-gradient estimates contain enough variability to accommodate most of the range in laboratory-derived Q values as summarized by Kirby (1980) but are definitely biased towards the hydrated olivine end. The most recent geotherm from Parsons & Sclater (1977) results from careful inversion of elevation, heat flow and age data from the North Atlantic and North Pacific. The major uncertainties in their model are the appropriate values for the specific heat and thermal conductivity. Assuming that their model is correct, the activation energy for ductile flow in the oceanic lithosphere cannot be greater than $100 \, \text{kcal mol}^{-1}$. From laboratory analogies this result would imply a hydrolytically weakened lithosphere at 40 km depth, but some petrologists would argue that oceanic basalts, high in FeO and low in Al_2O_3, result from shallow fractionation in a dry system (Kay, Hubbard & Gast 1970).

The low Q values found here need not necessarily imply a conflict with the petrochemistry of basalt genesis. We have assumed that the activation energy (Q_L or Q_H) in the flow equations (9) and (10) is the only uncertain parameter, but the pre-exponential B values and the stress exponent n are also empirically determined constants. Although we chose to examine the effect on the yield criteria of Q alone because the exponential dependence makes the equations more sensitive to small changes in Q, published estimates of B_1 vary by orders of magnitude and n generally ranges between 3 and 3.7 (see Kirby 1980, table 2). A careful examination of the reported parameters, however, shows that B_1, Q and n do not vary independently. Large B_1 values correspond to low n values, and the observed link between B_1 and Q can be quantified by a compensation law (Lasaga 1981; Tsukahara 1976) derived from the theoretical and empirical connection between dislocation climb and creep (Weertman 1970).

The net effect of these trade-offs is that within the narrow range of experimental conditions ($1100°C < T < 1600°C$, $\dot{\epsilon} \approx 10^{-5} \, \text{s}^{-1}$), essentially similar data sets can be fit by only slightly different curves which nevertheless correspond to very different B_1, Q and n values. Very often in these studies Q was more or less assigned a value near $125 \, \text{kcal mol}^{-1}$ as an article of faith based upon a predicted equivalence between the activation energies for creep and preliminary data for diffusion from Goetze & Kohlstedt (1973). Beyond the range of experimental conditions, in the lower T, lower $\dot{\epsilon}$ region of interest here, these empirical curves can rapidly diverge, but the laboratory data will not determine which is correct because obviously no experimentalist will be around long enough to observe creep in olivine at 500°C. There is no guarantee that equations with the functional form of (9) and (10) will even be adequate to fit observations over a larger temperature range.

Our approach of allowing Q to vary does seem to be justified in retrospect. The low value we find for low T, low $\dot{\epsilon}$ ductile flow in the oceanic lithosphere is supported by recent laboratory experiments. For a wider range of temperatures, the relationship between stress and strain rate cannot be expressed by a single Q values, but rather with a Q decreasing with decreasing T (Durham 1975; Kirby 1980). Impurities occurring under natural conditions also tend to lower Q.

Conclusions

The most important parameter influencing the mechanical thickness of the oceanic lithosphere is its age, but estimates of mechanical thickness as a function of age will be underestimated if plate curvature and finite yield strength are not taken into account. For trench profiles, the consideration of curvature is especially crucial. A 40 km thick plate with curva-

ture $8 \times 10^{-7} \, \text{m}^{-1}$ and yield strength shown in Fig. 7 would appear to be only 29 km thick in the context of an elastic rheology.

In comparing observed estimates of moment and curvature to the predictions from theoretical yield envelopes, it appears that the lithospheric is weaker than laboratory extrapolations taken at face value. Of the possible weakening mechanisms, elevated pore-fluid pressure on faults in the zone of brittle failure is not likely to be the primary agent unless we invoke some age-dependence in the extent of pore-fluid effects. We conclude that either the oceanic geotherm is steeper than commonly assumed, or the activation energy for ductile deformation is significantly lower than the value for dry dunite at high temperature.

Some final comments are in order regarding the limitations of this sort of analysis. For bathymetric profiles surrounding seamounts, it is hardly necessary to go beyond the simple elastic plate formulation. As seen in Fig. 9, the plate curvature is low enough that the effects of finite yield strength are unimportant. Immediately beneath the loads the more extreme curvature in the plate which could be observed in the deflection of the Moho or other density discontinuity might require a more sophisticated analysis. For trench profiles, even seaward of the steep outer trench wall curvatures are large enough to warrant the use of strength-limiting rheologies in order to avoid the erroneous conclusion that sharply-bent plates are physically thinner. The moment/curvature formulation as outlined here is useful only to the extent that variations in moment arising from differences in curvature, temperature, and strain rate can be approximated by changes in the elastic thickness; i.e. we have restricted ourselves to profiles of the form in equation (13). However, because the method requires that we choose plate parameters to satisfy flexure data from many different examples simultaneously, it reduces some of the non-uniqueness inherent in studies which attempt to model the entire length of a single profile numerically with a non-linear rheology. Nowhere have we shown that the yield envelope in Fig. 7 actually explains the deformation along an entire trench profile, but hopefully it can be used as a starting point for such detailed investigations.

Acknowledgments

References

Abramowitz, M. & Stegun, I. A., 1965. *Handbook of Mathematical Functions with Formulas, Graphs, and Mathematical Tables,* National Bureau of Standards Applied Mathematics Series 55, US Government Printing Office, Washington, DC, 1046 pp.

Anderson, W. L., 1979. Computer program – numerical integration of related Hankel transforms of orders 0 and 1 by adaptive digital filtering, *Geophysics,* **44,** 1287–1305.

Bodine, J. H., Steckler, M. S. & Watts, A. B., 1981. Observations of flexure and the rheology of the oceanic lithosphere, *J. geophys. Res.,* **86,** 3695–3707.

Bodine, J. H. & Watts, A. B., 1979. Lithospheric flexure seaward of the Bonin and Mariana trenches, *Earth planet. Sci. Lett.,* **43,** 132–148.

Brace, W. F. & Kohlstedt, D. L., 1980. Limits on lithospheric stress imposed by laboratory experiments, *J. geophys. Res.,* **85,** 6248–6252.

Brotchie, J. F. & Silvester, R., 1969. On crustal flexure, *J. geophys. Res.,* **74,** 5240–5252.

Byerlee, J. D., 1968. Brittle-ductile transition in rocks, *J. geophys. Res.,* **73,** 4741–4750.

Byerlee, J. D., 1978. Friction of rocks, *Pageoph,* **116,** 615–626.

Caldwell, J. G., 1979. The mechanical behaviour of the oceanic lithosphere near subduction zones, *PhD thesis,* Cornell University, 151 pp.

Caldwell, J. G., Haxby, W. F., Karig, D. E. & Turcotte, D. L., 1976. On the applicability of a universal elastic trench profile, *Earth planet. Sci. Lett.*, **31**, 239–246.

Carey, E. & Dubois, J., 1981. Behaviour of the oceanic lithosphere at subduction zones; plastic yield strength from a finite element method, *Tectonophys.*, **74**, 99–110.

Cathles, L. M., 1975. *The Viscosity of the Earth's Mantle*, Princeton University Press, Princeton, New Jersey, 386 pp.

Chapple, W. M. & Forsyth, D. W., 1979. Earthquakes and bending of plates at trenches, *J. geophys. Res.*, **84**, 6729–6749.

Cochran, J. R., 1979. An analysis of isostasy in the world's oceans: 2. Mid-ocean ridge crests, *J. geophys. Res.*, **84**, 4713–4729.

Dalrymple, G. B., 1971. Potassium-argon ages on the Polohu volcanic series, *Bull. geol. Soc. Am.*, **82**, 1997–2000.

Detrick, R. S. & Crough, S. T., 1978. Island subsidence, hot spots, and lithospheric thinning, *J. geophys. Res.*, **83**, 1236–1244.

Durham, W. B., 1975. Plastic flow of single crystal olivine, *PhD thesis*, Massachusetts Institute of Technology, Boston.

Evans, B. & Goetze, C., 1979. The temperature variation of hardness of olivine and its implication for polycrystalline yield stress, *J. geophys. Res.*, **84**, 5505–5524.

Furumoto, A. S., Wollard, G. P., Campbell, J. F. & Hussong, D. M., 1968. Variations in the thickness of the crust in the Hawaiian archipelago, in *The Crust and Upper Mantle of the Pacific Area*, pp. 94–111, eds Knopoff, L., Drake, C. & Hart, P., *Geophys. Monogr. Am. geophys. Un. 12*, Washington, DC.

Gantmacher, F. R., 1960. *The Theory of Matrices*, translated from Russian by K. A. Hirsch, vols 1 and 2, Chelsea Publishing Co., New York.

Goetze, C., 1978. The mechanisms of creep in olivine, *Phil. Trans. R. Soc. A*, **288**, 99–119.

Goetze, C. & Evans, B., 1979. Stress and temperature in the bending lithosphere as constrained by experimental rock mechanics, *Geophys. J. R. astr. Soc.*, **59**, 463–478.

Goetze, C. & Kohlstedt, D. L., 1973. Laboratory studies of dislocations climb and diffusion in olivine, *J. geophys. Res.*, **78**, 5961–5971.

Hamilton, E. L., 1957. Marine geology of the southern Hawaiian ridge, *Bull. geol. Soc. Am.*, **68**, 1011–1026.

Hanks, T. C., 1971. The Kuril Trench–Hokkaido Rise system: large shallow earthquakes and simple models of deformation, *Geophys. J. R. astr. Soc.*, **23**, 173–189.

Jones, G. M., Hilde, T. W. C., Sharman, G. F. & Agnew, D. C., 1978. Fault patterns in outer trench walls and their tectonic significance, *J. Phys. Earth*, **26**, S85–S101.

Kay, R. Hubbard, N. J. & Gast, P. W., 1970. Chemical characteristics and origin of oceanic ridge volcanic rocks, *J. geophys. Res.*, **75**, 1585–1613.

Kirby, S. H., 1977. State of stress in the lithosphere: Inferences from the flow laws of olivine, *Pure appl. Geophys.*, **115**, 245–258.

Kirby, S. H., 1980. Tectonic stresses in the lithosphere: constraints provided by the experimental deformation of rocks, *J. geophys. Res.*, **85**, 6353–6363.

Lasaga, A. C., 1981. The atomistic basis of kinetics: defects in minerals, in *Reviews in Mineralogy*, **8**, 261–319, eds Lasaga, A. C. & Kirkpatrick, R. J.

Liu, H.-P., 1980. The structure of the Kuril–Hokkaido rise system computed from an elastic time-dependent plastic model incorporating rock deformation data, *J. geophys. Res.*, **85**, 901–912.

McAdoo, D. C., Caldwell, J. G. & Turcotte, D. L., 1978. On the elastic-perfectly plastic bending of the lithosphere under generalized loading with application to the Kuril trench, *Geophys. J. R. astr. Soc.*, **54**, 11–26.

McKenzie, D. P., 1967. Some remarks on heat flow and gravity anomalies, *J. geophys. Res.*, **72**, 6261–6273.

McKenzie, D. P. & Bowin, C., 1976. The relationship between bathymetry and gravity in the Atlantic Ocean, *J. geophys. Res.*, **81**, 1903–1915.

McNutt, M. K., 1979. Compensation of oceanic topography: an application of the response function technique to the *Surveyor* area, *J. geophys. Res.*, **84**, 7589–7598.

McNutt, M. K. & Menard, H. W., 1978. Lithospheric flexure and uplifted atolls, *J. geophys. Res.*, **83**, 1206–1212.

McNutt, M. K. & Menard, H. W., 1979. Reply to comments by Jarrard and Turner on 'Lithospheric flexure and uplifted atolls', *J. geophys. Res.*, **84**, 5695–5697.

Menard, H. W. & McNutt, M. K., 1982. Evidence for and consequences of thermal rejuvenation, *J. geophys. Res.*, in press.

Mercier, J.-C. & Carter, N. L., 1975. Pyroxene geotherms, *J. geophys. Res.*, **80**, 3349–3362.

Mercier, J.-C., Carter, N. L. & Anderson, D., 1977. Stress in the lithosphere: Inferences from steady-state flow of rocks, *Pure appl. Geophys.*, **115**, 199–226.

Parker, R. L. & Oldenburg, D. W., 1973. A thermal model of ocean ridges, *Nature*, **242**, 137–139.

Parsons, B. & Sclater, J., 1977. An analysis of the variation of ocean floor bathymetry and heat flow with age, *J. geophys. Res.*, **82**, 803–827.

Post, R. L., 1977. High temperature creep of Mt. Burnette dunite, *Tectonophys.*, **42**, 75–110.

Sclater, J. G. & Francheteau, 1970. The implications of terrestrial heat-flow observations on current tectonic and geochemical models of the crust and upper mantle of the earth, *Geophys. J.*, **20**, 509–542.

Sclater, J. G., Parsons, B. & Jaupart, C., 1981. Oceans and continents: Similarities and differences in the mechanisms of heat loss, *J. geophys. Res.*, **86**, 11 535–11 552.

Suyenaga, W., 1977. Earth deformation in response to surface loading: application to the formation of the Hawaiian Ridge, *PhD thesis*, University of Hawaii, 147 pp.

Swanson, D. A., 1972. Magma supply rate at Kilauea volcano, 1952–1971, *Science*, **175**, 169–170.

Turcotte, D. L. & Oxburgh, E. R., 1967. Finite-amplitude convection cells and continental drift, *J. Fluid Mech.*, **28**, 29–42.

Tsukahara, H., 1976. Diffusion and diffusion creep in olivine and ultrabasic rocks, *J. Phys. Earth*, **24**, 89–103.

Vening-Meinesz, F. A., 1941. Gravity over the Hawaiian Archipelago and over the Madeira area, *Proc. K. ned. Akad. Wet.*, 44 pp.

Walcott, R. I., 1970. Flexure of the lithosphere at Hawaii, *Tectonophys.*, **9**, 435–446.

Watts, A. B., 1978. An analysises of isotasy in the world's oceans: 1. Hawaiian–Emperor seamount chain, *J. geophys. Res.*, **83**, 5989–6004.

Watts, A. B., Bodine, J. H. & Ribe, N. R., 1980. Observations of flexure and the geologic evolution of the Pacific ocean basin, *Nature*, **238**, 532–537.

Watts, A. B. & Cochran, J. R., 1974. Gravity anomalies and flexure of the lithosphere along the Hawaiian–Emperor seamount chain, *Geophys. J. R. astr. Soc.*, **38**, 119–141.

Watts, A. B., Cochran, J. R. & Selzer, G., 1975. Gravity anomalies and flexure of the lithosphere: a three-dimensional study of the Great Meteor seamount, North-east Atlantic, *J. geophys. Res.*, **80**, 1391–1398.

Watts, A. B. & Talwani, M., 1974. Gravity anomalies seaward of deep-sea trenches and their tectonic implications, *Geophys. J. R. astr. Soc.*, **36**, 57–90.

Weertman, J., 1970. The creep strength of the earth's mantle, *Rev. Geophys. Space Phys.*, **8**, 145–168.

Appendix A

The expressions for w, w_b, x_b, M and K given in the main text correspond to the solutions for bending a thin elastic plate under a line load with infinitesimal thickness in the x-direction. Here we derive the corresponding solutions for other loading cases and demonstrate the similarity in the resulting equations for M and K when expressed in terms of w_b and x_b.

RECTANGULAR LOAD

Consider a two-dimensional load with rectangular cross-section and half-width L, height h, density ρ_0, resting on an elastic plate with flexural parameter

$$\alpha = \sqrt[4]{4D/\Delta\rho g}$$

in which D is the flexural rigidity and $\Delta\rho$ is the density contrast between fluids above and beneath the plate. The equations describing the plate deflection are

$$D\, d^4 w/dx^4 + \Delta\rho g w = -\rho_0 g h \qquad \text{for} \qquad x \leqslant L, \tag{A1}$$

$$D\, d^4 w/dx^4 + \Delta\rho g w = 0 \qquad \text{for} \qquad x \geqslant L. \tag{A2}$$

We seek inner and outer solutions w_i and w_o to (A1) and (A2), respectively, subject to the following boundary conditions:

$$w_o(\infty) = 0,$$

$$w_i'(0) = 0,$$

$$w_i(L) = w_o(L),$$

$$w_i'(L) = w_o'(L),$$

$$w_i''(L) = w_o''(L).$$

The solutions are:

$$w_i = \frac{h\rho_0}{\Delta\rho} \exp(-L/\alpha) \left[\cos\frac{L}{\alpha} \cos\frac{x}{\alpha} \cosh\frac{x}{\alpha} + \sin\frac{L}{\alpha} \sin\frac{x}{\alpha} \sinh\frac{x}{\alpha} - 1 \right],$$

$$w_o = \frac{-h\rho_0}{\Delta\rho} \exp(-x/\alpha) \left[\cos\frac{L}{\alpha} \sinh\frac{L}{\alpha} \cos\frac{x}{\alpha} + \sin\frac{L}{\alpha} \cosh\frac{L}{\alpha} \sin\frac{x}{\alpha} \right].$$

Let

$$H = -h\rho_0/\Delta\rho,$$

$$F_1 = \cos L/\alpha \ \sinh L/\alpha,$$

$$F_2 = \sin L/\alpha \ \cosh L/\alpha,$$

then

$$w_o = H \exp(-x/\alpha) (F_1 \cos x/\alpha + F_2 \sin x/\alpha). \tag{A3}$$

The zeros of (A3) occur at

$$x/\alpha = \tan^{-1}(-F_1/F_2). \tag{A4}$$

The maximum in the arch occurs at

$$\frac{F_1}{F_2} = \frac{\cos x/\alpha - \sin x/\alpha}{\cos x/\alpha + \sin x/\alpha}$$

for which the solution is

$$x/\alpha = \tan^{-1}(-F_1/F_2) + \pi/4. \tag{A5}$$

We see from (A4) and (A5) that the spacing between consecutive zeros is $\pi\alpha$ and the arch peaks at a distance $\pi\alpha/4$ from the first node, just as in the point load solution. Furthermore, these conclusions hold for any other loading geometry, although the expressions for F_1 and F_2 will be different.

We can shift the origin of the coordinate system so that it lies at the first zero crossing:

$$u/\alpha = x/\alpha - \tan^{-1}(-F_1/F_2).$$

Now (A3) becomes

$$w_o(u) = -H \exp\{-\tan^{-1}(-F_1/F_2)\} \exp(-u/\alpha) \sin u/\alpha. \tag{A6}$$

The arch occurs at $u_b = \pi\alpha/4$ and has amplitude

$$w_b = -H \exp\{-\tan^{-1}(-F_1/F_2)\} \exp(-\pi/4) \sin \pi/4.$$

In terms of w_b, (A6) becomes

$$w_0(u) = w_b \sqrt{2} \exp(\pi/4) \exp(-u/\alpha) \sin u/\alpha \tag{A7}$$

which is identical to equation (13) when the constant A is replaced by the expression for w_b. Therefore, the equations for the moment (14) and curvature (15) also apply for the line load case with arbitrary loading geometry landward of the first zero crossing. The effect of distributing the load is to reduce the amplitude of the arch by the factor $\exp[-\tan^{-1}(-F_1/F_2)]$, thereby reducing the moment also. This damping factor become appreciable for $L > \alpha$. It is trivial to show that (14) and (15) also apply for the case in which the plate is fractured underneath the load.

POINT LOAD

The deflection of a thin elastic plate beneath a point load is

$$w(r) = -(P l^2/2\pi D) \, kei \, r/l \tag{A8}$$

in which P is the weight of the load, $l = \sqrt[4]{D/\Delta\rho g}$, and kei is a modified Bessel function. The moment at the position r is

$$M = -D(d^2 w/dr^2 + v/r \, dw/dr),$$

$$= P/2\pi \, [ker \, r/l - (1-v)/(r/l) \, kei' \, r/l]$$

in which ker is another modified Bessel function and kei' is the first derivative of kei. The first zero crossing x_0 occurs at $r/l = 3.91467$ (Abramowitz & Stegun 1965) and the movement there is

$$M(x_0) = -0.00704 \, P. \tag{A9}$$

At the peak in the arch,

$$r/l = 4.93181$$

$$w_b = 0.01122 \, Pl^2/(2\pi D).$$

Since $x_b = 1.01714$, we can express (A8) in terms of w_b and x_b:

$$M = \Delta\rho g \, (-0.04421/0.01122) \, w_b \, x_b^2 \tag{A10}$$

from which we obtain equations (17) and (19).

Similarly for the curvature,

$$K = d^2 w/dr^2 + 1/r \, dw/dr$$

$$= (P/2\pi D) \, (ker \, r/l + l/r \, kei' \, r/l)$$

and at the first zero crossing,

$$K(x_0) = (P/2\pi D) \, (-0.0289).$$

In terms of x_b and w_b,

$$K(x_0) = (-0.0289/0.0112) \, w_b/x_b^2$$

from which we obtain (18) and (20).

CYLINDRICAL LOAD

Now suppose we consider a cylindrical load of height h and radius R. Again we must solve for inner and outer solutions, matching the two at the edge of the load. The outer solution is (Brotchie & Silvester 1969)

$$w_o(r) = H(F_3 \, ker \, r/l - F_4 \, kei \, r/l) \tag{A11}$$

in which

$$H = \rho_0 h/\Delta\rho,$$

$$F_3 = R/l \, ber' \, R/l,$$

$$F_4 = R/l \, bei' \, R/l,$$

which is similar in form to (A3). Nevertheless, it is not possible to cast (A11) exactly into the form of (A8) and show that identical expressions hold for M and K in terms of x_b and w_b, as we did for the rectangular load case. Modified Bessel functions such as ker and kei are not as well behaved as sines and cosines in the sense that it is not possible to replace $ker \, x$ by $kei \, (x + \omega)$ where ω is some phase angle. The zeros of (A11) will not have constant spacing, independent of F_3 and F_4. Fortunately in the region of the rise, the values for r/l are large enough (> 4) so that asymptotic expressions for ker and kei in terms of trigonometric functions are accurate to within a few per cent:

$$ker \, x = N \cos\phi,$$

$$kei \, x = N \sin\phi,$$

$$N \simeq \sqrt{\pi/2x} \, \exp(-x/\sqrt{2}),$$

$$\phi \simeq -x/\sqrt{2} - \pi/8.$$

We will demonstrate that these trigonometric approximations to (A8) and (A11) provide a sufficiently accurate alternative to the Bessel function solution at distances beyond the first nodal point and produce almost identical expressions for M and K in terms of x_b and w_b for both point and cylindrical loading geometries.

The trigonometric approximation to (A8) is

$$w(r) = \frac{P}{\pi\Delta\rho g \alpha^2} \sqrt{\frac{\pi\alpha}{2\sqrt{2}r}} \, \exp(-r/\alpha) \sin(r/\alpha + \pi/8)$$

where $\sqrt{2} \, l = \alpha$. We shift the origin to the first node by setting

$$x/\alpha = r/\alpha - 7\pi/8$$

and obtain

$$w(x) = \frac{-P}{\pi\Delta\rho g \alpha^2} \sqrt{\frac{\pi}{2\sqrt{2}(x/\alpha + 7\pi/8)}} \, \exp(-7\pi/8) \exp(-x/\alpha) \sin x/\alpha.$$

The maximum in the arch occurs at

$$\tan x_b/\alpha = \left(1 + \frac{1}{2x_b/\alpha + 7\pi/4}\right)^{-1}$$

which can be solved numerically to yield

$$x_b = 0.7183\alpha = 1.016 \, l.$$

This value is within about 0.1 per cent of the x_b determined from (A8), $x_b = 1.017\,l$.

At the peak in the arch,

$$w_b = -0.1816 \exp(-7\pi/8) \, \frac{P}{\pi \Delta \rho g \alpha^2} = \frac{-0.0116\,P}{\pi \Delta \rho g \alpha^2} \, .$$

In terms of w_b,

$$w(x) = \frac{w_b}{0.1816} \sqrt{\frac{\pi}{2\sqrt{2}(x/\alpha + 7\pi/8)}} \exp(-x/\alpha) \sin x/\alpha. \tag{A13}$$

Expressions (A8) and (A13) are indistinguishable within the accuracy of any observations beyond the first node.

The asymptotic expression for the plate flexure caused by a cylindrical load (A11) is

$$w(r) = H \sqrt{\frac{\pi \alpha}{2\sqrt{2}r}} \exp(-r/\alpha) \, [F_3 \cos(r/\alpha + \pi/8) + F_4 \sin(r/\alpha + \pi/8)].$$

Again we shift the origin to the first node:

$$x/\alpha = r/\alpha - 7\pi/8 - \tan^{-1}(-F_3/F_4)$$

$$w(x) = -H \sqrt{\frac{\pi}{2\sqrt{2} \, \{x/\alpha + 7\pi/8 \, \tan^{-1}(-F_3/F_4)\}}} \exp\left[-\tan^{-1}(-F_3/F_4)\right]$$

$$\times \exp(-7\pi/8) \exp(-x/\alpha) \sin x/\alpha. \tag{A14}$$

The maximum in the arch occurs at

$$\tan x_b/\alpha = \left(1 + \frac{1}{2x_b/\alpha + 7\pi/8 + 2\,\tan^{-1}(-F_3/F_4)}\right)^{-1}$$

which is not identical to (A12) due to the additional factor $2 \tan^{-1}(-F_3/F_4)$. Fortunately, the solution for x_b is fairly insensitive to this parameter since R/l is small, of the order of 2 or less. For $R/l = 2$, $x_b = 1.022\,l$ which is within 1 per cent of the point load value, and

$$w_b = -0.1755\,H \exp\left[-\tan^{-1}(-F_3/F_4)\right] \exp(-7\pi/8).$$

In terms of w_b, (A14) becomes

$$w(x) = \frac{w_b}{0.1755} \sqrt{\frac{\pi}{2\sqrt{2}\,[x/\alpha + 7\pi/8 + \tan^{-1}(-F_3/F_4)]}} \exp(-x/\alpha) \sin x/\alpha. \tag{A15}$$

Let

$$C_p(x) = \frac{1}{0.1816} \sqrt{\frac{\pi}{2\sqrt{2}(x/\alpha + 7\pi/8)}}$$

$$C_c(x) = \frac{1}{0.1755} \sqrt{\frac{\pi}{2\sqrt{2}\,[x/\alpha + 7\pi/8 + \tan^{-1}(F_3/F_4)]}}$$

where C_p and C_c are the factors which differ in the point load (A13) and cylindrical load (A15) asymptotic solutions, respectively. Since C_c is within 2 per cent of C_p for $x > 0$, for our purposes (A13) and (A15) can be considered equivalent, and therefore estimates of M

and K in terms of x_b and w_b based on the point load approximation also apply to distributed loading geometries.

Appendix B

To estimate the volume of material comprising the island of Hawaii, its root and the moat infill we deform a thick elastic plate with a circularly symmetric Gaussian load. The plate thickness, load amplitude and load radius are adjusted until the resulting deformation agrees with the observed bathymetry and depth to the Moho in the vicinity of the island. The thick plate solution for bending an elastic plate beneath a surface load with circularly symmetric geometry parallels the development given by Cathles (1975) for a line load. Only an outline of the derivation is given here.

To approximate the case for seamount loading on the oceanic lithosphere, we adopt a cylindrical coordinate system with no $\hat{\theta}$ dependence:

$$u = u(r, z),$$

$$w = w(r, z),$$

where u and w are displacements in the radial and vertical directions, respectively. To be consistent with Cathles (1975), we choose $\hat{z}$ positive upward. In this coordinate system, the equations of equilibrium are:

$$\frac{\partial \tau_{rr}}{\partial r} + \frac{\partial \tau_{rz}}{\partial z} + \frac{\tau_{rr} - \tau_{\theta\theta}}{r} = 0,$$

$$\frac{\partial \tau_{rz}}{\partial r} + \frac{\tau_{rz}}{r} + \frac{\partial \tau_{zz}}{\partial z} = 0,$$

where τ_{ij} are the components of the stress tensor. The constitutive relations for a homogeneous elastic medium become:

$$\tau_{rr} = \lambda(\partial u/\partial r + u/r + \partial w/\partial z) + 2\mu \, \partial u/\partial r,$$

$$\tau_{rz} = \mu(\partial u/\partial z + \partial w/\partial r),$$

$$\tau_{zz} = \lambda(\partial u/\partial r + u/r + \partial w/\partial z) + 2\mu \, \partial w/\partial z,$$

$$\tau_{\theta\theta} = \lambda(\partial u/\partial r + u/r + \partial w/\partial z) + 2\mu \, u/r,$$

in which λ is Lame's constant and μ is the modulus of shear.

We define Hankel transforms $\mathcal{H}_0$ and $\mathcal{H}_1$ as

$$\mathcal{H}_0[f(r)] = \int_0^\infty f(r) \, J_0(kr) \, r \, dr$$

$$\mathcal{H}_1[f(r)] = \int_0^\infty f(r) \, J_1(kr) \, r \, dr.$$

After transforming the above equilibrium and stress/strain equations and eliminating τ_{rr}, we obtain

$$\frac{\partial \bar{u}}{\partial z} = k\bar{w} + \mu^{-1}\,\bar{\tau}_{rz}, \tag{A16}$$

$$\frac{\partial \bar{w}}{\partial z} = -\sigma^{-1}\lambda k\bar{u} + \sigma^{-1}\bar{\tau}_{zz}, \tag{A17}$$

$$\frac{\partial \bar{\tau}_{rz}}{\partial z} = 4\mu k^2 \sigma^{-1}(\lambda + \mu)\,\bar{u} + \sigma^{-1}k\lambda\bar{\tau}_{zz}, \tag{A18}$$

$$\frac{\partial \bar{\tau}_{zz}}{\partial z} = -k\bar{\tau}_{rz}, \tag{A19}$$

in which

$$\bar{u} = \mathcal{H}_1[u] \qquad\qquad \bar{\tau}_{zz} = \mathcal{H}_0[\tau_{zz}]$$

$$\bar{w} = \mathcal{H}_0[w] \qquad\qquad \sigma = \lambda + 2\mu$$

$$\bar{\tau}_{rz} = \mathcal{H}_1[\tau_{rz}].$$

In deriving the above equations we make use of the following identities which can be established by integration by parts:

$$\mathcal{H}_0[f'(r)] = k\,\mathcal{H}_1[f] - \mathcal{H}_0[f/r],$$

$$\mathcal{H}_1[f'(r)] = -k\,\mathcal{H}_0[f],$$

$$\mathcal{H}_0\left[\frac{1}{r}\frac{d}{dr}[rf(r)]\right] = k\,\mathcal{H}_1[f],$$

$$\mathcal{H}_1\left[\frac{1}{r}\frac{d}{dr}[rf(r)]\right] = \mathcal{H}_1\left[\frac{f}{r}\right] - k\,\mathcal{H}_0[f].$$

Except for the definition of the transformed variables $\bar{u}$, $\bar{w}$, $\bar{\tau}_{rz}$ and $\bar{\tau}_{zz}$, equations (A16)–(A19) are identical to those derived by Cathles (1975) for a line load. For the case of incompressible elasticity ($\lambda \to \infty$), the system of equations becomes

$$\partial_z \begin{pmatrix} 2k\bar{u} \\ 2k\bar{w} \\ \bar{\tau}_{rz} \\ \bar{\tau}_{zz} \end{pmatrix} = \begin{pmatrix} 0 & 1 & 2\mu^{-1} & 0 \\ -1 & 0 & 0 & 0 \\ 2 & 0 & 0 & 1 \\ 0 & 0 & -1 & 0 \end{pmatrix} \begin{pmatrix} 2k\bar{u} \\ 2k\bar{w} \\ \bar{\tau}_{rz} \\ \bar{\tau}_{zz} \end{pmatrix}.$$

The above set of equations is in the form

$$\partial \vec{v}/\partial z = \overleftrightarrow{A}\vec{v}$$

so that at least schematically we can write the solution as

$$\vec{v}(z) = \exp\{\overleftrightarrow{A}z\}\,\vec{v}(z_0)$$

in which $\vec{v}(z_0)$ contains the initial values of displacement and stress at the boundary of the elastic layer. The matrix

$$\vec{P} = \exp\{\vec{A}z\}$$

is the propagator matrix which relates displacement and stress at any depth z in a homogeneous elastic layer to the values at the surface. For a layered medium in which the elastic parameters vary in the vertical direction only, the solution at z_b, the base of the layers, is

$$\vec{v}(z_b) = \vec{P}_n \vec{P}_{n-1} \vec{P}_{n-2} \dots \vec{P}_2 \vec{P}_1 \vec{v}(z_0).$$

Each $\vec{P}_i$ propagates the solution at the top of the layer to the bottom of the layer.

The form of the matrix $\vec{P}$ is completely determined by the eigenvalues of $\vec{A}$ (Gantmacher 1960). For a homogeneous, imcompressible elastic layer,

$$\begin{pmatrix} \bar{u}(z) \\ \bar{w}(z) \\ \bar{\tau}_{rz(z)} \\ \bar{\tau}_{zz(z)} \end{pmatrix} = \begin{pmatrix} CP & C & SP/2\mu k & S/2\mu k \\ -C & CM & -S/2\mu k & SM/2\mu k \\ 2\mu kSP & 2\mu kS & CP & C \\ -2\mu kS & 2\mu kSM & -C & CM \end{pmatrix} \begin{pmatrix} \bar{u}(0) \\ \bar{w}(0) \\ \bar{\tau}_{rz}(0) \\ \bar{\tau}_{zz}(0) \end{pmatrix} \qquad \text{(A20)}$$

$SP = \sinh kz + kz \cosh kz,$

$CP = \cosh kz + kz \sinh kz,$

$SM = \sinh kz - kz \cosh kz,$

$CM = \cosh kz - kz \sinh kz,$

$S = kz \sinh kz,$

$C = kz \cosh kz.$

Closed-form solutions for displacement and stress can be derived for simple layered models such as an elastic or linear viscoelastic plate over an inviscid or viscous fluid with load either held constant in time or steadily increasing or decreasing in time. Here we only report the result for an elastic plate with thickness T_e overlying an inviscid fluid. For a seamount load, the boundary conditions are:

$$\bar{\tau}_{rz}(0) = \bar{\tau}_{rz}(-T_e) = 0,$$

$$\bar{\tau}_{zz}(-T_e) = \Delta\rho g\bar{u}(-T_e)$$

in which $\Delta\rho$ is the density contrast between fluids overlying and underlying the plate. Physically these boundary conditions state that a fluid responds with buoyancy pressures and sustains no shear stress. Substituting these boundary conditions into the propagator matrix equations (A20), after six pages of algebra we obtain

$$\bar{u}(0) = \frac{k'2 - \Delta\rho gT/2\mu}{\sinh k' + k' \cosh k'} \, \bar{w}(-T_e),$$

$$\bar{w}(0) = \frac{\sinh k' \cosh k' + k' + (\Delta\rho g/2\mu k) \sinh^2 k'}{\sinh k' + k' \cosh k'} \, \bar{w}(-T_e),$$

$$\bar{\tau}_{zz}(0) = \frac{\Delta\rho g(\sinh k' \cosh k' + k') + 2\mu k(\sinh^2 k' - k'^2)}{\sinh k' + k' \cosh k'} \, \bar{w}(-T_e),$$

$$\bar{w}(0) = \frac{\sinh k' \cosh k' + k' + (\Delta\rho g/2\mu k) \sinh^2 k'}{2\mu k(\sinh^2 k' - k'^2) + \Delta\rho g(\sinh k' \cosh k' + k')} \, \bar{\tau}_{zz}(0) \tag{A21}$$

in which $k' = kT_e$. Again, except for the definitions of the transforms, these solutions agree with those of Cathles (1975) to within the accuracy of typographical errors.

We can confirm that in the limit of small k' (thin plate relative to the wavelength of deformation) these solutions reduce to the thin plate equations. To order k'^3,

$$\bar{w}(0) = \left(1 - \frac{\Delta\rho g T_e}{4\mu}\right) \bar{w}(-T_e)$$

$$\bar{u}(0) = \frac{-\Delta\rho g T_e}{4\mu} \bar{w}(-T_e)$$

$$\bar{w}(-T_e) = \left(1 + \frac{\mu k^4 T_e^3}{3\Delta\rho g}\right)^{-1} \frac{\bar{\tau}_{zz}}{\Delta\rho g} \, .$$

Assuming reasonable values for $\Delta\rho, g, T_e$, and μ,

$$\frac{\Delta\rho g T_e}{4\mu} \ll 1.$$

Therefore, we recover the thin plate equations:

$$\bar{w}(0) = \bar{w}(-T_e) = \left(1 + \frac{\mu k^4 T_e^3}{3\Delta\rho g}\right) \frac{\bar{\tau}_{zz}(0)}{\Delta\rho g} \, .$$

$$\bar{u}(0) \ll \bar{w}(-T_e).$$

Equation (A21) can be used to determine the elastic deformation at the surface of a plate caused by a circularly symmetric stress distribution τ_{zz}. To simulate a volcanic island, we chose τ_{zz} of the form

$$\tau_{zz} = -\rho_0 g H \exp(-r^2/\beta^2)$$

and used a digital Hankel transform (Anderson 1979) to calculate $\bar{\tau}_{zz}$ and $\mathcal{H}_0^{-1}[\bar{w}]$. We allowed H, β and T_e to vary until the final profile of the plate deflection and load roughly displayed the following features:

    (1) average height of the island above sea-level = 3.5 km;
    (2) height of island from moat to sea-level = 5.4 km;
    (3) distance from load to arch = 300 km;
    (4) radius of island at sea-level = 55 km;
    (5) radius of island at base = 120 km;
    (6) depth from sea-level to Moho = 15 km (or 8 km to top of plate).

Sources for these values are Hamilton (1957), Furumoto *et al.* (1968) and Walcott (1970). The values for $\rho_0, \Delta\rho$ and μ were set at $1800 \, \text{kg m}^{-3}$, $2300 \, \text{kg m}^{-3}$ and $2.7 \times 10^{10} \, \text{N m}^{-2}$, respectively.
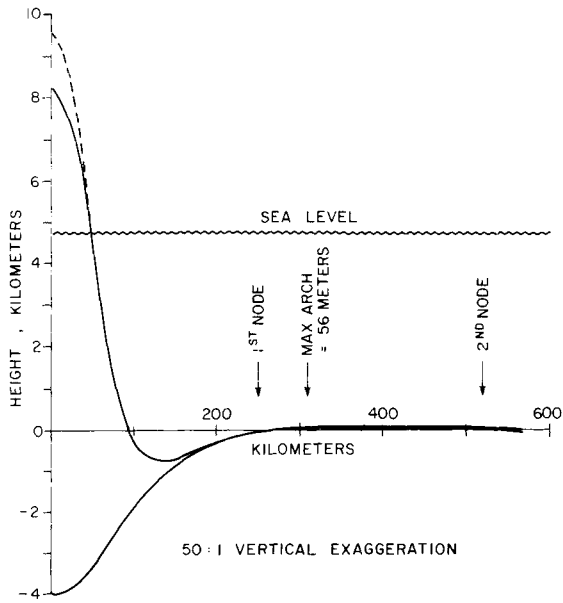
Figure A1. Cross-section through a circularly symmetric load resting on an elastic plate. The upper solid curve shows the bathymetry while the lower solid curve shows the deflection of the upper surface of the deformed plate. The dashed curve is the configuration of the original Gaussian stress distribution which has been corrected downward to the bathymetric outline to account for a greater effective density of subaerial basalt.

The preferred solution, shown in Fig. A1, is in reasonable agreement with these observations. The most serious discrepancy is in the model's overestimation of the height difference between the moat and arch (800 m instead of 600 m). However, a few hundred metres of low-density sediment could be added to the moat without changing the plate flexure significantly. Alternatively, the superposition of a long-wavelength swell peaking near the load would tend to reduce the observed moat-arch height difference. The parameters in the preferred solution are:

$H = 13.5$ km,

$\beta = 70$ km,

$T_e = 30$ km.

To obtain a volume estimate for Hawaii, we note that

$$V = 2\pi H \int_0^\infty \exp(-r^2/\beta^2)\, r\,dr$$

$$= \pi\beta^2 H$$

$$= 2.08 \times 10^5 \text{ km}^3.$$